

Entropic depletion of DNA in triangular nanochannels

Wesley F. Reinhart, Douglas R. Tree, and Kevin D. Dorfman^{a)}

Department of Chemical Engineering and Materials Science, University of Minnesota–Twin Cities, 421 Washington Ave. SE, Minneapolis, Minnesota 55455, USA

(Received 21 January 2013; accepted 14 February 2013; published online 1 March 2013)

Using Monte Carlo simulations of a touching-bead model of double-stranded DNA, we show that DNA extension is enhanced in isosceles triangular nanochannels (relative to a circular nanochannel of the same effective size) due to entropic depletion in the channel corners. The extent of the enhanced extension depends non-monotonically on both the accessible area of the nanochannel and the apex angle of the triangle. We also develop a metric to quantify the extent of entropic depletion, thereby collapsing the extension data for circular, square, and various triangular nanochannels onto a single master curve for channel sizes in the transition between the Odijk and de Gennes regimes. © 2013 American Institute of Physics. [<http://dx.doi.org/10.1063/1.4794371>]

I. INTRODUCTION

Understanding the extension of polymers in two dimensional confinement (i.e., in nanochannels) has become especially important in recent years in the context of single molecule genomic mapping of DNA.^{1–8} Rectangular nanochannels or approximations thereof are by far the most widespread experimental geometry, since these shapes are amenable to standard lithographic techniques. In an intriguing alternate approach, Huh *et al.*⁹ showed that mechanical deformation of cracked polydimethylsiloxane (PDMS) leads to isosceles triangular nanochannels, where the apex angle and the size of the nanochannels depend on the strain applied to the material. Similar strategies have been used to create triangular nanochannels to stretch DNA or control its transport rate.^{9–12} In the present contribution, we show that the extension of DNA in these triangular nanochannels can be mapped onto the models developed for circular and rectangular nanochannels, provided that we account for the role of the corners in a triangular channel.

In our analysis, we will focus on nanochannels of characteristic size D , which lie between the Odijk regime¹³ of strong confinement ($D \lesssim l_p$, where l_p is the persistence length of the chain) and the de Gennes regime¹⁴ of weak confinement ($l_p^2/w \lesssim D \lesssim R_g$, where w is the effective width of the DNA and R_g is its radius of gyration). These sizes are the relevant range for most experimental data.^{7,15} Previous simulation work^{15–19} indicates that the average extension of DNA in square nanochannels in this transition regime scales with the channel size as

$$\langle X \rangle \sim D_{\text{eff}}^{-1}, \quad (1)$$

where $D_{\text{eff}} \equiv D - w$ is the effective channel size available to a chain with finite width w . Alternatively, we could consider an effective area $A_{\text{eff}} \sim D_{\text{eff}}^2$, as illustrated in Fig. 1(a). If the scaling law in Eq. (1) is robust with respect to the channel shape, then

$$\langle X \rangle \sim A_{\text{eff}}^{-1/2}. \quad (2)$$

However, Odijk²⁰ suggested that the stiffness of the chain leads to entropic depletion from the corners. This idea is illustrated in the schematic of Fig. 1(a), where the DNA can more easily

^{a)}dorfman@umn.edu.

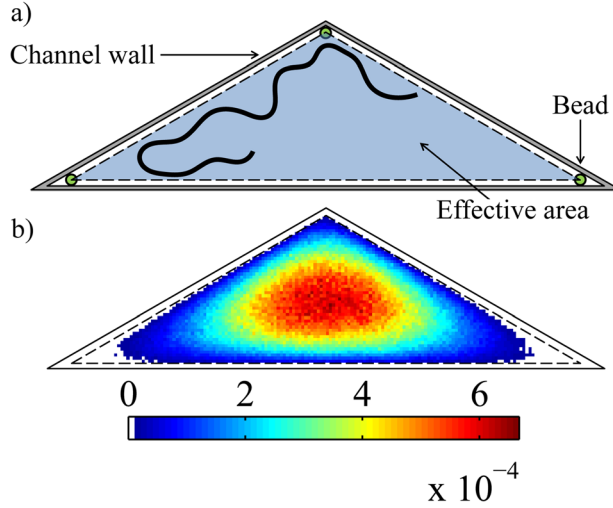


FIG. 1. (a) Schematic representation of an isosceles triangular channel in our simulations. The DNA is represented by beads with hardcore excluded volume interactions with one another and the walls. The area of the channel that is accessible to the bead centers (bounded by the dashed line) is the effective area. The thick black curve schematically depicts a portion of a DNA molecule projected onto the channel cross-section. The semiflexible nature of the chain decreases the probability of having a high radius of curvature and therefore restricts the chain from fitting easily into the corners of the channel. (b) A probability density plot from our simulations (see Sec. II) for an apex angle of 120° . The effective area boundary from panel (a) is included for reference. Note the entropic depletion in the corners caused by the bending penalty illustrated in (a), which increases as the angle of the corner decreases.

bend to fit into the corner with the larger angle. To be precise, the number of configurations available near a corner is reduced by the penalty for bending the DNA on a length scale commensurate with its persistence length. If entropic depletion is substantial, then D_{eff} is no longer the proper length scale and Eq. (2) is not valid.

In what follows, we use Monte Carlo simulations of confined DNA^{15,21} to show that entropic depletion indeed plays an important role in a triangular nanochannel, as seen in the simulation data in Fig. 1(b). Entropic depletion increases the extension relative to a circular nanochannel with the same value of A_{eff} . Unfortunately, this result renders Eq. (2) invalid for triangular nanochannels. We construct a new length scale, F_{av} , that accounts for the entropic depletion and collapses all of the data for circular, square, and isosceles triangle nanochannels of different apex angles onto the scaling law

$$\langle X \rangle \sim F_{\text{av}}^{-1} \quad (3)$$

in the technologically relevant transition regime between the Odijk and de Gennes regimes.

II. SIMULATION METHOD

Our simulations employ the same model as our previous work for square nanochannels.²¹ Briefly, the DNA backbone is represented by a series of touching beads of diameter $w = 4.6$ nm, the Stigter effective width for DNA in TBE $5\times$ buffer,^{15,20} and the commonly invoked persistence length $l_p = 53$ nm.²² The chain has $N = 1024$ beads, giving a contour length $L = 4.7$ μm . The beads exhibit hardcore excluded volume interactions with one another and with the channel walls. The persistence length is implemented by a discrete wormlike chain bending potential²³

$$\frac{U_{\text{bend}}}{k_B T} = \frac{l_p}{w} \sum_{k=1}^{N-2} (1 - \vec{u}_k \cdot \vec{u}_{k+1}) \quad (4)$$

applied to adjacent beads, where \vec{u}_k is the unit vector from the center of bead k to that of bead $k+1$, k_B is Boltzmann's constant, and T is the temperature.

Configurations were generated by a Metropolis Monte Carlo simulation using pivot, crankshaft, and reptation moves. Simulations for each channel were performed in parallel using 4 replicates. For a given configuration, we computed the span, $X = \max(x_i) - \min(x_i)$, where x_i is the position of the i th bead in the direction along the channel axis. We use the mean span,¹⁵ $\langle X \rangle$, as the measure of the average chain extension, since this is the experimentally relevant parameter. To determine an appropriate sampling interval, we calculated its auto-covariance function,²⁴

$$C_{\langle X \rangle}(n) = \frac{\langle X(m)X(m+n) \rangle_m - \langle X \rangle^2}{\langle X^2 \rangle - \langle X \rangle^2}. \quad (5)$$

We found that a sampling interval of $n = 2.048 \times 10^7$ trial moves yields a sufficiently low auto-correlation in the majority of the simulated channels without significantly under-sampling in large channels. Each simulation run was initialized from a straight chain and allowed to equilibrate for 1.024×10^8 trial moves before recording configurations. Each replicate produced 250 statistically independent configurations, yielding 10^3 total configurations per channel.

We performed simulations in isosceles triangle nanochannels with apex angles from 15° to 165° in increments of 15° , keeping the effective area A_{eff} constant. These simulations were repeated for six different values of A_{eff} . Circular channels were simulated for the same effective areas and several additional values. Square channels were simulated at selected effective areas for comparison. Since much of the data in the figures overlap, tabulated data of the effective areas, corresponding fractional extensions and the standard error for each measurement are also reported.²⁵

III. RESULTS AND DISCUSSION

We begin our analysis by testing whether the scaling in Eq. (2) captures the simulated extension data. As we would expect from similar simulations,^{15–19} the data for the circular channels and square channels in Fig. 2 are well approximated by the scaling law for sensible values of the fractional extension, $\langle X \rangle/L \gtrsim 0.2$. Note that our chains do not possess sufficient contour length ($L \cong l_p^3/w^2$) required to enter the de Gennes regime.¹⁵ Thus, the data for small extensions in Fig. 2 correspond to a transition from confinement to the bulk.¹⁵

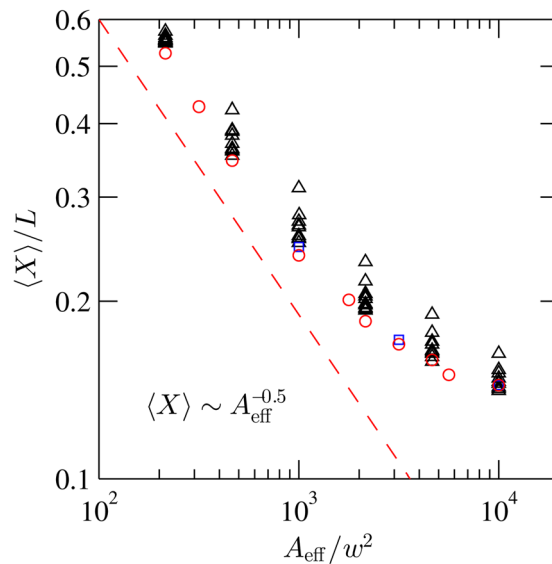


FIG. 2. Fractional mean span plotted as a function of the effective area. Black triangles are triangular channels with different apex angles, red circles are circular channels, blue squares are square channels. The symbols' sizes are proximate to the standard error. The dashed line shows the scaling of Eq. (2). For completeness, the data are tabulated.²⁵

The data in Fig. 2 indicate the failure of cross-sectional area to adequately predict DNA extension in triangular channels; even in the steepest portion of the curve, the same extension was attained in channels with effective areas differing by a factor of two by changing the apex angle. Indeed, channels with the same effective area but different shape or apex angle vary in mean span by as much as 20%. This deviation is statistically significant, since the standard error in the measurement of the chain extension is around 1%. In comparison, the largest discrepancy between circles and squares is only 3%, essentially within the statistical error.

In general, a triangular nanochannel leads to increased extension when compared to a circular channel with the same effective area. The extent of this increase, plotted in Fig. 3 as a relative extension with respect to the circular channel, depends on both the effective area of the channel and the apex angle. For the smallest channel, the relative extension is modest and relatively insensitive to the apex angle. As the channel size increases, we observe two distinct patterns. First, there is a general trend in the relative extension with varying apex angle, leading to a global maximum at the largest apex angle, a broad minimum region somewhere around an equilateral triangle, and a local maximum at the smallest apex angle. Second, the enhancement in the stretching is non-monotonic in effective area. In the left panel, corresponding to the smaller channels, the enhancement increases with A_{eff} . In the right panel, corresponding to the larger channels, the enhancement decreases with A_{eff} . These trends in Fig. 3 are also apparent in Fig. 2, with the circles and triangles essentially overlapping for our largest and smallest channels.

The entropic depletion concept²⁰ explains the trends with apex angle and channel size in Fig. 3. It is easiest to understand the principle of entropic depletion by comparing the cross-sectional distribution of segments in a circular channel, which has no corners, to a square channel. Figure 4 shows the probability densities $p(y, z)$ for different channels with a fixed value of $A_{\text{eff}} = 10^3 w^2$, created by binning the configuration data into pixels of size $6.25 \times 10^{-2} w^2$. For the circular cross-section, nearly the entire channel is sampled with a probability density of at least 10^{-6} . The white edge ($p < 10^{-6}$) of the probability density near the wall indicates the excluded area resulting from the finite diameter of the beads, analogous to the schematic in Fig. 1(a). Most of the roughness around the edge of the plot comes from intentional pixelation to achieve smooth interpolations. The circular channel has no corners, so there cannot be any entropic depletion due to a corner. In contrast, entropic depletion caused by the physical corners in the square channel leads to rounded corners in the probability density. The region where the probability of sampling was below 10^{-6} extends from the vertex to a point outside the region

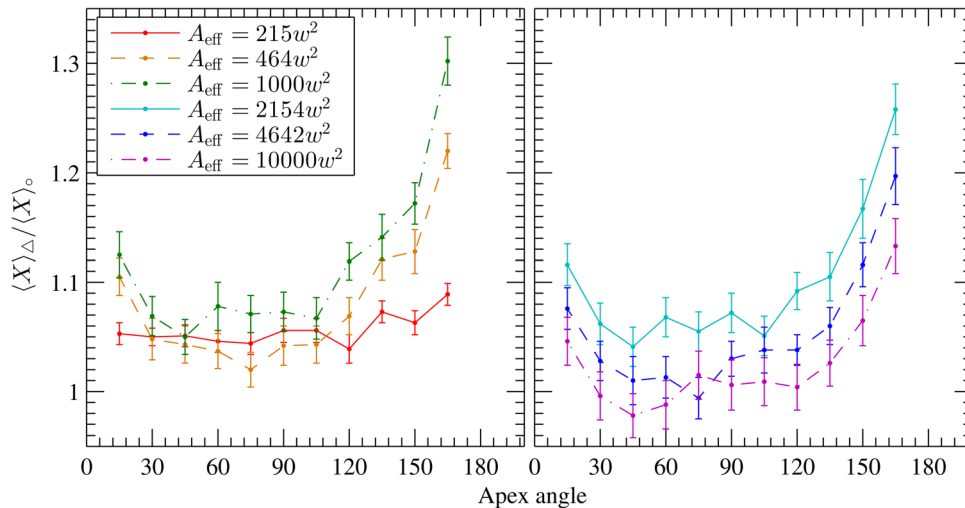


FIG. 3. Mean span in triangles normalized by that of a circular channel of equal effective area as a function of apex angle in the triangle. The particular values of A_{eff} are listed in the legend. The data are separated into two panels for clarity. The relative extension increases with A_{eff} in the left panel and decreases with A_{eff} in the right panel.

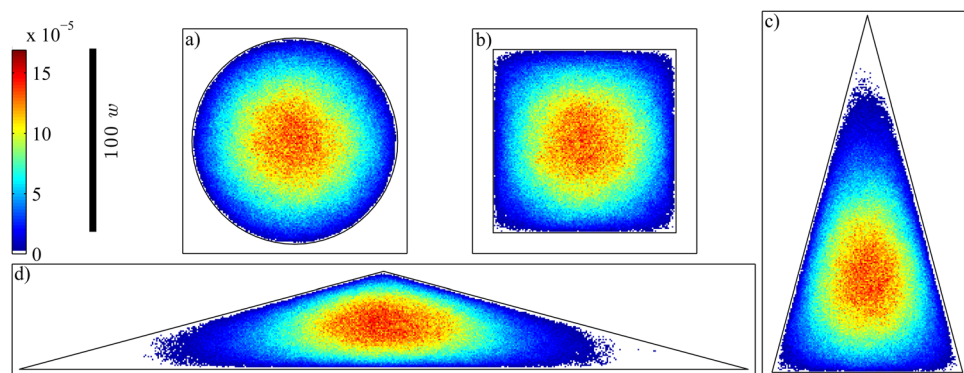


FIG. 4. Probability density plots of channels with effective area $A_{\text{eff}} = 10^3 w^2$ created by binning the configuration data into pixels of size $6.25 \times 10^{-2} w^2$. Black lines indicate channel boundaries. If the probability density in the pixel is less than 10^{-6} , the pixel is white. (a) Circular channel. (b) Square channel. (c) Triangular channel with apex angle 30° . (d) Triangular channel with apex angle 150° .

of hardcore excluded volume interactions with the wall. The entropic depletion effect also propagates into the channel somewhat, leading to rounding of the inner contours of the probability density. However, the bulk of the probability density (at the center of the channel) exhibits a circular symmetry that is consistent with blob theory¹⁴ and essentially the same as the probability density for the circular channel. Thus, while there is some entropic depletion due to the corners in a square channel, the net effect is small. Indeed, the limited entropic depletion and circularly symmetric probability density in a square channel explain the excellent agreement between scaling theories, which do not account for the channel geometry, and simulations in square and rectangular channels.^{15–19} The details of the channel geometry are adsorbed into minor changes to the scaling law prefactor, at least until the rectangle becomes so anisotropic that it begins to approach a slit.¹⁴

In contrast to the circular and square nanochannels, the triangular nanochannels in Fig. 4 feature substantial entropic depletion near an acute angle. Naturally, there is minimal entropic depletion near an obtuse angle since the DNA can easily bend to fit into such a corner. Indeed, the probability density near an obtuse angle is similar to that near the perimeter of the circle in Fig. 4(a). The extent of the entropic depletion increases as the angle of the corner decreases, thereby explaining the non-monotonic relationship between the relative extension and apex angle in Fig. 3—the global maximum in the enhanced stretching is achieved with two depleted corners (large apex angle), the local maximum is achieved with one depleted corner (small apex angle), and the least entropic depletion occurs when there are no small corners (equilateral triangle).

Entropic depletion also produces the non-monotonic dependence of the enhanced stretching as a function of the effective area, but the origin of this trend is more subtle than the trend in the apex angle. Entropic depletion is a local effect; the chain is depleted from a region near the corner because the penalty for bending into the corner is large compared to thermal energy. However, the extent to which the entropic depletion in the corner affects the extension of the chain depends on how easily a subsection of the chain can coil in the center of the channel. For the smallest channel in our simulations, the chain can hardly coil in the center of the channel due to its stiffness. At this lower limit, there is a slight increase in the extension due to entropic depletion, but the enhanced stretching is insensitive to the apex angle. As the channel size increases, the role of the entropic depletion becomes more important since the chain is able to coil in the center of the channel. Here, the available configurations for part of the chain in the corner are distinctly different than those available to the same section of the chain if it was in the center of the channel. Eventually, the channel size becomes so large that we reach the unconfined (bulk) limit. At this upper limit, all relative extensions should approach unity since the polymer is no longer aware of the channel shape or size. Since both the lower and

upper limits in channel size have minimal entropic depletion, there must be a maximum in the relative extension versus effective area at a moderate channel size.

While the stretching of the chain depends on the geometry of the triangle, Fig. 5 shows that the distribution of the chain density in the axial direction is independent of the apex angle. To create this distribution, we computed the span X for each sampled chain configuration and then normalized the axial position x of each bead in that chain with its span. For a given apex angle, we can then construct a probability density in this normalized coordinate system by binning the data for all of the samples. In this way, we are able to collapse the data for all apex angles into a single plot. The symmetry of Fig. 5 arises from the arbitrary choice of the labels for the end/start of the chain. The highest segment density is at the ends of the chain, where the excluded volume interactions are small. The plateau in the segment density starting from $x/X = 0.5$ and extending outward corresponds to the segment density we would expect to see for an infinite chain with no end effects. The collapse of the data for all of the apex angles also confirms that the chains are long enough to be stretched in the axial direction even for the largest and smallest apex angles. While these channels appear slit-like in their cross-section, the entropic depletion from the corners makes them appear dramatically less anisotropic to the DNA.

The data in Fig. 3 embody the key practical result of our analysis. These curves provide the map from results for circular channels, which are relatively easy to obtain, to triangular nanochannels. Moreover, the data suggest that the triangular channels from Huh *et al.*⁹ are close to the region where one benefits the most from entropic depletion. In their DNA experiments, the channels were approximated as isosceles triangles with an apex angle of roughly 155° and an effective area $A_{\text{eff}} \approx 600w^2$, close to the channel area exhibiting the best stretching enhancement in Fig. 3. Our simulation data also agree well with the experimental value of $\langle X \rangle / L = 0.3$ obtained in these experiments.⁹

From a fundamental perspective, we would also like to have a method for collapsing all of the extension data in Fig. 2 onto a single master curve. We propose to use the characteristic length scale of the probability distribution, rather than the size of the channel, in order to account for the entropic depletion from the corners. To determine this size, we first compute the eigenvectors of the covariance matrix for the bead coordinates projected onto a plane whose normal vector points down the channel axis. We then use a bilinear interpolation function to evaluate the observed probability density along each of the eigenvectors. For smoothness and consistency, the bin size of the probability density is scaled inversely to the logarithm of A_{eff} such that the bin size of the smallest channel is 36 pixels/ w^2 and the largest is 4 pixels/ w^2 . The interpolated data series are then fit with 4th degree polynomials to smooth the data. Figure 6

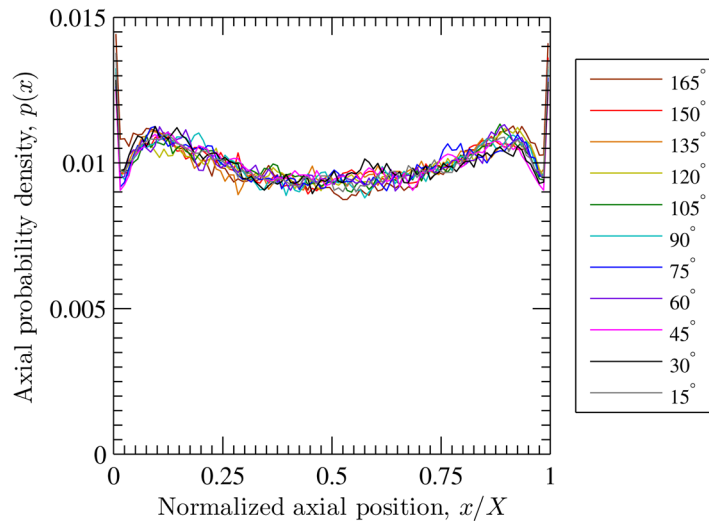


FIG. 5. Axial chain density distributions for triangular channels with $A_{\text{eff}} = 10^3 w^2$. Positions are normalized by the span X of each configuration. Each bin has a width of 1% of the total span. Lines are different apex angles.

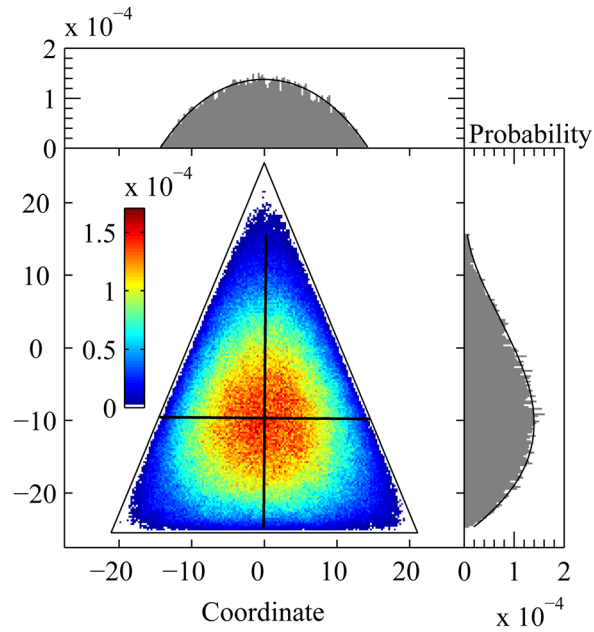


FIG. 6. A probability density plot from the simulation for an apex angle of 45° . The eigenvectors of the covariance of the projected bead positions are overlaid in black. Interpolated data from each of the eigenvectors are shown as histograms in the adjacent panels (vertical on the right, horizontal on top). Lines in the side panels are 4th degree polynomial regressions of data sets. The geometric average of the full width at half maximum of the polynomials is defined as F_{av} .

shows one example of the data generated by this algorithm. Since the distribution is different on the two eigenvectors, we take a geometric average of the full width at half maximum of the fitted polynomials for each eigenvector and define this quantity F_{av} as the length scale for the probability distribution. The results for F_{av} for all of the nanochannels, obtained using this approach, are tabulated.²⁵

By plotting mean span against our calculated F_{av} , we see a collapse of the data along a single curve. In contrast to Fig. 2, the data in Fig. 7 show a smooth power-law scaling $\langle X \rangle \sim F_{av}^{-1}$

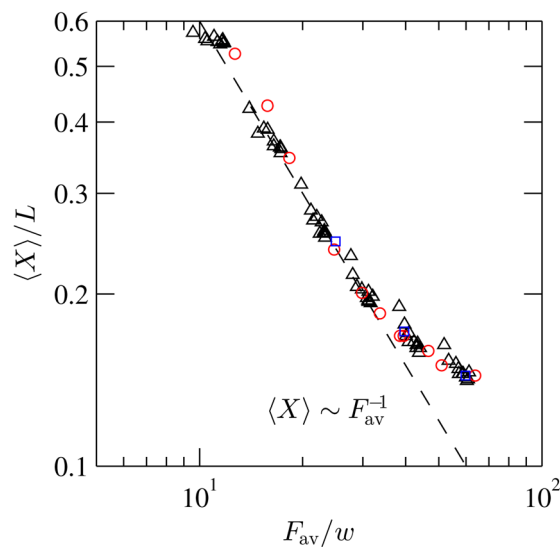


FIG. 7. Fractional extension plotted as a function of the characteristic size of the probability density in the channel cross-section, F_{av} . Black triangles are triangular channels, red circles are circular channels, and blue squares are square channels. Symbols are sized proximate to the standard error. The dashed line shows -1 scaling. Tabulated data are also available.²⁵

with the same prefactor for circles, squares, and triangles. As we noted in the context of Fig. 2, we do not expect to see a de Gennes regime for this short chain, since it cannot form isometric blobs.^{15,26}

IV. CONCLUDING REMARKS

We have demonstrated that DNA confinement in isosceles triangular nanochannels leads to enhanced DNA stretching, when compared to an equivalent size circular channel, and that the extent of this enhanced stretching depends on the apex angle and size of the nanochannel. The sharp corners lead to entropic depletion therein, which gives rise to a non-monotonic behavior in the extension as a function of the apex angle. Our simulation results also provide insight into the entropic effects in corners, a phenomenon which has received little attention so far.²⁰

While we are able to obtain a description of chain extension in triangular confinement that collapses the data, our approach should be regarded as a phenomenological description rather than generic approach for predicting DNA extension in complex geometries. Based on Fig. 7, it seems that F_{av} is the relevant length scale to describe a channel-confined polymer in the transition between the Odijk and de Gennes regimes. However, computing this quantity requires the cross-sectional probability distribution, data which would be virtually impossible to acquire in an experiment. Furthermore, if the spatial coordinates of each segment of the polymer are already known, then the mean span is also known. Until there is an *a priori* approach to compute F_{av} for a given channel geometry, we view our approach and the data obtained here²⁵ as a useful reference for experimental design, rather than a comprehensive theoretical framework.

Although we focused exclusively on the extension of the chain in a triangular nanochannel, it is reasonable to assume that the hydrodynamic mobility of the chain will also be affected by the channel shape. In the transition between the Odijk and de Gennes regimes, we might expect that the hydrodynamic mobility will decrease in a triangular channel (when compared to the equivalent circular channel) due to the viscous dissipation in the corners of the channel. However, if we move to even smaller channels in the Odijk regime, we might expect the hydrodynamic mobility to increase in a triangular channel because the lubrication layer between the chain and the channel is thicker in the corners. Ultimately, these questions need to be resolved by detailed calculations of the fluid flow¹⁸ that are well beyond the scope of this paper. Indeed, calculating such flows can be challenging due to the sharp corners and the lower symmetry when compared to a rectangular channel. In this case, sophisticated hydrodynamic simulation methods for confined polymers²⁷ are probably necessary.

ACKNOWLEDGMENTS

We thank Professor Shuichi Takayama (University of Michigan) for sharing his experimental insights into this problem. This work was supported by the NIH (R01-HG005216) and was carried out in part using computing resources at the University of Minnesota Supercomputing Institute.

- ¹R. Riehn, M. Lu, Y. M. Wang, S. F. Lim, E. C. Cox, and R. H. Austin, *Proc. Natl. Acad. Sci. U.S.A.* **102**, 10012 (2005).
- ²K. Jo, D. M. Dhingra, T. Odijk, J. J. de Pablo, M. D. Graham, R. Runnheim, D. Forrest, and D. C. Schwartz, *Proc. Natl. Acad. Sci. U.S.A.* **104**, 2673 (2007).
- ³S. K. Das, M. D. Austin, M. C. Akana, P. Deshpande, H. Cao, and M. Xiao, *Nucleic Acids Res.* **38**, e177 (2010).
- ⁴Y. Kim, K. S. Kim, K. L. Kounovsky, R. Chang, G. Y. Jung, J. J. de Pablo, K. Jo, and D. C. Schwartz, *Lab Chip* **11**, 1721 (2011).
- ⁵K. H. Rasmussen, R. Marie, J. M. Lange, W. E. Svendsen, A. Kristensen, and K. U. Mir, *Lab Chip* **11**, 1431 (2011).
- ⁶E. T. Lam, A. Hastie, C. Lin, D. Ehrlich, S. K. Das, M. D. Austin, P. Deshpande, H. Cao, N. Nagarajan, M. Xiao, and P. Y. Kwok, *Nat. Biotechnol.* **30**, 771 (2012).
- ⁷W. Reisner, J. N. Pedersen, and R. H. Austin, *Rep. Prog. Phys.* **75**, 106601 (2012).
- ⁸K. D. Dorfman, S. B. King, D. W. Olson, J. D. P. Thomas, and D. R. Tree, "Beyond gel electrophoresis: Microfluidic separations, fluorescence burst analysis, and DNA stretching," *Chem. Rev.* (published online).
- ⁹D. Huh, K. L. Mills, X. Zhu, M. A. Burns, M. D. Thouless, and S. Takayama, *Nature Mater.* **6**, 424 (2007).
- ¹⁰E. Angeli, C. Manneschi, L. Repetto, G. Firpo, and U. Valbusa, *Lab Chip* **11**, 2625 (2011).
- ¹¹P. Fanzio, V. Mussi, C. Manneschi, E. Angeli, G. Firpo, L. Repetto, and U. Valbusa, *Lab Chip* **11**, 2961 (2011).
- ¹²P. Fanzio, C. Manneschi, E. Angeli, V. Mussi, G. Firpo, L. Cesaracci, L. Repetto, and U. Valbusa, *Sci. Rep.* **2**, 791 (2012).
- ¹³T. Odijk, *Macromolecules* **16**, 1340 (1983).

- ¹⁴M. Daoud and P. G. de Gennes, *J. Phys. (Paris)* **38**, 85 (1977).
- ¹⁵Y. Wang, D. R. Tree, and K. D. Dorfman, *Macromolecules* **44**, 6594 (2011).
- ¹⁶P. Cifra, *J. Chem. Phys.* **131**, 224903 (2009).
- ¹⁷P. Cifra, Z. Benková, and T. Bleha, *J. Phys. Chem. B* **113**, 1843 (2009).
- ¹⁸D. R. Tree, Y. Wang, and K. D. Dorfman, *Phys. Rev. Lett.* **108**, 228105 (2012).
- ¹⁹P. Cifra, *J. Chem. Phys.* **136**, 024902 (2012).
- ²⁰T. Odijk, *J. Chem. Phys.* **125**, 204904 (2006).
- ²¹Y. Wang, W. F. Reinhart, D. R. Tree, and K. D. Dorfman, *Biomicrofluidics* **6**, 014101 (2012).
- ²²C. Bustamante, J. F. Marko, E. D. Siggia, and S. B. Smith, *Science* **265**, 1599 (1994).
- ²³J. Wang and H. Gao, *J. Chem. Phys.* **123**, 084906 (2005).
- ²⁴W. Reisner, K. J. Morton, R. Riehn, Y. M. Wang, Z. Yu, M. Rosen, J. C. Sturm, S. Y. Chou, E. Frey, and R. H. Austin, *Phys. Rev. Lett.* **94**, 196101 (2005).
- ²⁵See supplementary material at <http://dx.doi.org/10.1063/1.4794371> for tabulated simulation data.
- ²⁶T. Odijk, *Phys. Rev. E* **77**, 060901(R) (2008).
- ²⁷Y. Zhang, J. J. de Pablo, and M. D. Graham, *J. Chem. Phys.* **136**, 014901 (2012).